

# Flight Demonstration of High Altitude Aircraft Navigation with Cellular Signals

Zaher M. Kassas, Joe Khalife, Ali Abdallah, Chiawei Lee, Juan Jurado, Steven Wachtel, Jacob Duede, Zachary Hoeffner, Thomas Hulsey, Rachel Quirarte, and RunXuan Tay

**Abstract**—This article presents the first demonstration of navigation with cellular signals of opportunity (SOPs) on a high altitude aircraft. An extensive flight campaign was conducted by the Autonomous Systems Perception, Intelligence, and Navigation (ASPIN) Laboratory in collaboration with the US Air Force (USAF) to sample ambient downlink cellular SOPs in different regions in Southern California, USA. Carrier phase measurements were produced from these signals, which were subsequently fused in an extended Kalman filter (EKF) along with altimeter measurements to estimate the aircraft’s state (position, velocity, and time). Three flights are performed in three different regions: (i) rural, (ii) semi-urban, and (iii) urban. A multitude of flight trajectories and altitudes above ground level (AGL) were exercised in the three flights: (i) a 51 km trajectory of grid maneuvers with banking and straight segments at about 5,000 ft AGL, (ii) a 57 km trajectory of a teardrop descent from 7,000 ft AGL down to touchdown at the runway, and (iii) a 55 km trajectory of a holding pattern at about 15,000 ft AGL. The estimated aircraft trajectory is computed for each flight and compared with the trajectory from the aircraft’s on-board navigation system, which utilized a GPS receiver coupled with an inertial navigation system (INS) and an altimeter. Cellular SOPs produced remarkable sustained navigation accuracy over the entire flight trajectories in all three flights, achieving a three-dimensional position root mean-squared error (RMSE) of 10.53 m, 4.96 m, and 15.44 m, respectively.

## I. INTRODUCTION

A quick search of the phrase “Global Positioning System (GPS)” on the aviation safety reporting system (ASRS) returns 579 navigation-related incidents since January 2000. The ASRS is a publicly available reporting system established by NASA to identify and address issues reported by frontline personnel in the aviation system [1]. A deeper look at the data reveals that out of these 579 incidents, a malfunction or failure was detected in navigation sensors with the following occurrences: 508 in “GPS & Other Satellite Navigation,” 34 in “Navigational Equipment and Processing,” 14 in “Flight Dynamics Navigation and Safety,” 12 in “Altimeter,” and 6 in “Positional/Directional Sensing.” Among these incidents, 100 are suspected to be due to GPS jamming and interference,

This work was supported in part by the Office of Naval Research (ONR) under Grant N00014-19-1-2511 and Grant N00014-19-1-2613; in part by Sandia National Laboratories under Award 1655264, in part by the National Science Foundation (NSF) under Grant 1929965; and in part by the U.S. Department of Transportation (USDOT) under Grant 69A3552047138 for the CARMEN University Transportation Center (UTC).

Z. Kassas, J. Khalife, and A. Abdallah are with the University of California, Irvine. C. Lee, J. Jurado, S. Wachtel, J. Duede, Z. Hoeffner, T. Hulsey, and R. Quirarte are with the US Air Force, USA. R. Tay is with the Republic of Singapore Air Force, Singapore. (Corresponding author: Z. Kassas, email: zkassas@ieee.org).

leading to the loss of the main and auxiliary GPS units in some cases. What is alarming is the increasing trend of GPS interference—the majority of the aforementioned incidents took place since 2019. What is more, previously undisclosed Federal Aviation Administration (FAA) data for a few months in 2017 and 2018 detail hundreds of aircraft losing GPS reception. On a single day in March 2018, 21 aircraft reported GPS problems to air traffic controllers near Los Angeles, California, USA [2]. These and other incidents uncover the vulnerabilities of existing aircraft navigation systems, which are highly dependent on global navigation satellite system (GNSS) signals and their augmentation systems (e.g., ground-based augmentation system (GBAS) and space-based augmentation system (SBAS)) [3], [4]. There is an urgent need for complementary robust and accurate navigation systems to ensure aviation safety.

In 2019, the International Civil Aviation Organization (ICAO) issued a Working Paper titled “An Urgent Need to Address Harmful Interferences to GNSS,” where it concluded that harmful RFI to GNSS would prevent the full continuation of safety and efficiency benefits of GNSS-based services. Moreover, there was a call for supporting multi-disciplinary development of alternative positioning, navigation, and timing strategy and solutions to complement the use of GNSS in aviation [5]. In 2021, the U.S. Department of Transportation released the “Complementary Positioning, Navigation, and Timing (PNT) and GPS Backup Technologies Demonstration Report” to Congress. The report concluded that while there are suitable, mature, and commercially available technologies to back up or to complement GPS, none of these systems alone can universally back up the PNT capabilities provided by GPS and its augmentations, necessitating a diverse universe of PNT technologies [6]. Moreover, in 2021, the National Institute of Standards and Technology (NIST) issued a report on “Foundational PNT Profile: Applying the Cybersecurity Framework for the Responsible Use of PNT Services,” where it identified signals of opportunity and terrestrial RF sources (e.g., cellular) as a mitigation category that apply to the PNT profile [7].

Among terrestrial RF signals of opportunity (SOPs), cellular signals have shown tremendous potential as an alternative PNT source [8] due to their inherently desirable attributes:

- Abundance: cellular base stations are abundant in most locales, with the number of base stations slated to increase dramatically with future cellular generations.
- Geometric diversity: cellular base stations are placed in favorable geometric configurations by construction of the

cellular infrastructure.

- Frequency diversity: in contrast to GNSS signals, cellular signals are transmitted at a wide range of frequencies, which makes more difficult to be simultaneously jammed or spoofed.
- High received power: received cellular carrier-to-noise (CNR) ratio is commonly tens of dBs higher than that of GNSS signals, even in deep urban canyons and indoor environments [9].
- High bandwidth: downlink cellular signals can be up to 20 MHz (in 4G long-term evolution (LTE)) and even higher in future generations, which yields precise time-of-arrival (TOA) estimates.
- Free to use: the cellular infrastructure is already operational; thus, with specialized receivers, navigation observables (pseudorange, carrier phase, and Doppler) can be extracted from the “always on” transmitted signals.

Recent results have shown the ability of cellular SOPs to yield meter-level-accurate navigation on ground vehicles [10], [11] in urban environments and submeter-level-accurate navigation on UAVs [12], [13]. Moreover, the robustness and availability of cellular SOPs have been demonstrated in a GPS-jammed environment [14].

Assessing cellular signals for aerial vehicles have been the subject of several studies recently [15]. These studies span radio channel modeling [16], [17]; evaluation of signal quality in terms of received signal power [18], [19], interference from cellular transmitters [20]–[22], and coverage and connectivity [23]–[25]; and standards recommendations [26], [27]. However, the majority of these studies focused on evaluating cellular signals for communication purposes with little attention to evaluating them for navigation purposes [28]. Moreover, they considered UAVs flying at low altitudes (up to 500 ft) and slow speeds (up to 50 km/h). A recent study revealed that cellular signals can be acquired and tracked at altitudes as high as 23,000 ft above ground level (AGL) and at horizontal distances of more than 100 km from cellular transmitters [29]. However, the potential of cellular SOPs for high altitude aircraft navigation has not been thoroughly assessed. This article aims to perform the first assessment of cellular SOPs for aircraft navigation by addressing the following question: Can cellular SOPs be received and exploited at aircraft altitudes to produce a robust navigation solution?

To answer this question, an *unprecedented* aerial flight campaign was conducted in March 2020 by the Autonomous Systems Perception, Intelligence, and Navigation (ASPIN) Laboratory in collaboration with the United States Air Force (USAF) at the Edwards Air Force Base (AFB), California, USA. The cellular software-defined radios (SDRs) of the ASPIN Laboratory were flown over on a USAF Beechcraft C-12 Huron, a fixed-wing aircraft, to collect ambient cellular signals. This unique dataset consists of combinations of flight runs over three different environments (rural, semi-urban, and urban) with altitudes ranging up to 23,000 feet and a multitude of trajectories and maneuvers including straight segments, banking turns, holding patterns, and ascending and descending teardrops performed by members of the USAF Test Pilot School (TPS). During these large-scale experiments, terabytes

of samples of 3G code division multiple access (CDMA) and 4G LTE signals were recorded under various conditions.

This article provides the first extensive demonstrations of their kind of utilizing cellular SOPs for navigation purposes on high altitude aircraft. The aim of these demonstrations is to show that should GNSS signals become unavailable or unreliable mid-flight, cellular SOPs could be used to produce a sustained and accurate navigation solution over trajectories spanning tens of kilometers.

To demonstrate the feasibility of aircraft navigation with cellular SOPs, three flights are performed in three different regions: (i) rural, (ii) semi-urban, and (iii) urban. A multitude of flight trajectories and altitudes above ground level (AGL) were exercised in the three flights: (i) a 51 km trajectory of grid maneuvers with banking and straight segments at about 5,000 ft AGL, (ii) a 57 km trajectory of a teardrop descent from 7,000 ft AGL down to touchdown at the runway, and (iii) a 55 km trajectory of a holding pattern at about 15,000 ft AGL.

The aircraft’s trajectory is estimated for each flight exclusively from cellular SOPs using an extended Kalman filter (EKF). The estimated aircraft trajectory is compared with the aircraft’s on-board navigation system, which used a GPS-aided inertial navigation system (INS) and an altimeter. Cellular SOPs produced remarkable navigation accuracy in all three flights, achieving a position root mean-squared error (RMSE) of 10.53 m, 4.96 m, and 15.44 m, respectively.

The rest of this article is organized as follows. Section II describes the aircraft dynamics and cellular SOP measurement model. Section III formulates the EKF navigation framework. Section IV describes the experimental setup with which the aircraft was equipped and overviews the environments in which the flight campaigns took place. Section V presents experimental aircraft navigation results exclusively with cellular signals. Section VI gives concluding remarks.

## II. MODEL DESCRIPTION

This section describes the aircraft dynamics and cellular SOP measurement models used in the rest of the article.

### A. Aircraft Dynamics Model

Depending on the aircraft’s motion and sensor suite, different dynamic models can be used to describe its dynamics. The goal of this article is to assess the minimum performance of aircraft navigation with cellular SOPs exclusively. As such, a simple, yet effective continuous Wiener process acceleration model is employed, which upon discretization at a constant sampling interval  $T$ , is given by

$$\mathbf{x}_{\text{pva}}(k+1) = \mathbf{F}_{\text{pva}} \mathbf{x}_r(k) + \mathbf{w}_{\text{pva}}(k), \quad k = 0, 1, 2, \dots, (1)$$

$$\mathbf{F}_{\text{pva}} = \begin{bmatrix} \mathbf{I}_{3 \times 3} & T\mathbf{I}_{3 \times 3} & \frac{T^2}{2}\mathbf{I}_{3 \times 3} \\ \mathbf{0}_{3 \times 3} & \mathbf{I}_{3 \times 3} & T\mathbf{I}_{3 \times 3} \\ \mathbf{0}_{3 \times 3} & \mathbf{0}_{3 \times 3} & \mathbf{I}_{3 \times 3} \end{bmatrix},$$

where  $\mathbf{x}_{\text{pva}} \triangleq [\mathbf{r}_r^\top, \dot{\mathbf{r}}_r^\top, \ddot{\mathbf{r}}_r^\top]^\top$ ,  $\mathbf{r}_r \triangleq [x_r, y_r, z_r]^\top$  is the 3-D position of the aircraft expressed in a North-East-Down

(NED) frame, and  $\mathbf{w}_{\text{pva}}$  is a discrete-time zero-mean white noise sequence with covariance  $\mathbf{Q}_{\text{pva}}$  given by

$$\mathbf{Q}_{\text{pva}} = \begin{bmatrix} \frac{T^5}{20} & \frac{T^4}{8} & \frac{T^3}{6} \\ \frac{T^4}{8} & \frac{T^3}{3} & \frac{T^2}{2} \\ \frac{T^3}{6} & \frac{T^2}{2} & T \end{bmatrix} \otimes \tilde{\mathbf{S}}_{\text{NED}},$$

where  $\otimes$  denotes the Kronecker product, and  $\tilde{\mathbf{S}}_{\text{NED}} \triangleq \text{diag}[\tilde{q}_N, \tilde{q}_E, \tilde{q}_D]$ , where  $\tilde{q}_N$ ,  $\tilde{q}_E$ , and  $\tilde{q}_D$  are the NED jerk continuous-time noise power spectra, respectively. It should be noted that more complicated dynamic models can be used to describe the aircraft's dynamics, e.g., Singer acceleration, mean-adaptive acceleration, circular motion, curvilinear motion, coordinated turn, among others [30]. Of course, if an INS is available, its measurements can be used to describe the aircraft's motion, while aiding the INS with cellular SOPs [31].

### B. Clock Error Dynamics Model

Wireless standards require cellular base stations to be synchronized to within a few microseconds, which is order of magnitudes higher than the nanosecond requirements in GNSS. As such, the base station clock errors, which are dynamic and stochastic, must be accounted for in the navigation filter when navigation with cellular SOPs. A typical model for the dynamics of the clock error states is the so-called two-state model, composed of the clock bias  $\delta t$  and clock drift  $\dot{\delta t}$ , given by

$$\mathbf{x}_{\text{clk}}(k+1) = \mathbf{F}_{\text{clk}} \mathbf{x}_{\text{clk}}(k) + \mathbf{w}_{\text{clk}}(k), \quad (2)$$

where  $\mathbf{w}_{\text{clk}}$  is a discrete-time zero-mean white noise sequence with covariance  $\mathbf{Q}_{\text{clk}}$ , and

$$\mathbf{F}_{\text{clk}} = \begin{bmatrix} 1 & T \\ 0 & 1 \end{bmatrix}, \quad \mathbf{Q}_{\text{clk}} = \begin{bmatrix} S_{\tilde{w}_{\delta t}} T + S_{\tilde{w}_{\dot{\delta t}}} \frac{T^3}{3} & S_{\tilde{w}_{\delta t}} \frac{T^2}{2} \\ S_{\tilde{w}_{\dot{\delta t}}} \frac{T^2}{2} & S_{\tilde{w}_{\dot{\delta t}}} T \end{bmatrix}. \quad (3)$$

The power spectra  $S_{\tilde{w}_{\delta t}}$  and  $S_{\tilde{w}_{\dot{\delta t}}}$  are determined by the quality of the oscillator from which the clock signal is derived [32].

### C. SOP Measurement Model

ASPIN Laboratory's SDR, called MATRIX: Multichannel Adaptive TRansceiver Information eXtractor, produces several types of navigation observables. In order to get the highest possible precision, carrier phase observables are exploited for navigation, which after some manipulations can be modeled as [14]

$$z_n(k) = \|\mathbf{r}_r(k) - \mathbf{r}_{s_n}\|_2 + c\delta t_n(k) + v_n(k), \quad n = 1, 2, \dots, N, \quad (4)$$

where  $\mathbf{r}_{s_n}$  is the  $n$ -th cellular base station's 3-D position vector;  $c$  is the speed of light;  $\delta t_n$  is the overall clock error in the  $n$ -th carrier phase measurement, which combines the effect of receiver and base station clock biases and the initial carrier phase ambiguity;  $N$  is the total number of available base stations; and  $v_n(k)$  is the measurement noise, which is modeled as a discrete-time zero-mean white Gaussian sequence with variance  $\sigma_n^2(k)$ . The measurement noise variance can be modeled as a function of the CNR [33], [34].

### D. Altimeter Measurement Model

Since cellular base stations appear to have similar altitudes for a high-flying aircraft, their vertical dilution of precision (VDOP) will be very large. To circumvent this issue, altimeter data  $z_{\text{alt}}$  derived from the aircraft's on-board navigation system is used in addition to the cellular carrier phase measurements in the measurement-update step in the EKF.

## III. NAVIGATION FRAMEWORK

This section formulates the EKF navigation framework based on the models presented in II.

### A. EKF Model

Let  $\mathbf{x} \triangleq [\mathbf{x}_{\text{pv}}^\top, \mathbf{x}_{\text{clk}_1}^\top, \dots, \mathbf{x}_{\text{clk}_N}^\top]^\top$  denote the state to be estimated, where  $\mathbf{x}_{\text{clk}_n} \triangleq [c\delta t_n, \dot{c\delta t}_n]^\top$ . Using (1) and (2), one can write the dynamics of  $\mathbf{x}$  as

$$\mathbf{x}(k+1) = \mathbf{F}\mathbf{x}(k) + \mathbf{w}(k), \quad (5)$$

where  $\mathbf{F} \triangleq \text{diag}[\mathbf{F}_{\text{pva}}, \mathbf{F}_{\text{clk}_1}, \dots, \mathbf{F}_{\text{clk}_N}]$  and  $\mathbf{w}(k)$  is the overall process noise vector, which is a zero-mean white sequence with covariance  $\mathbf{Q} \triangleq \text{diag}[\mathbf{Q}_{\text{pva}}, \mathbf{Q}_{\text{clk}}]$ , and

$$\bar{\mathbf{Q}}_{\text{clk}} \triangleq \begin{bmatrix} \mathbf{Q}_{\text{clk}_r} + \mathbf{Q}_{\text{clk}_{s_1}} & \mathbf{Q}_{\text{clk}_r} & \dots & \mathbf{Q}_{\text{clk}_r} \\ \mathbf{Q}_{\text{clk}_r} & \mathbf{Q}_{\text{clk}_r} + \mathbf{Q}_{\text{clk}_{s_2}} & \dots & \mathbf{Q}_{\text{clk}_r} \\ \vdots & \vdots & \ddots & \vdots \\ \mathbf{Q}_{\text{clk}_r} & \mathbf{Q}_{\text{clk}_r} & \dots & \mathbf{Q}_{\text{clk}_r} + \mathbf{Q}_{\text{clk}_{s_N}} \end{bmatrix},$$

where  $\mathbf{Q}_{\text{clk}_r}$  and  $\{\mathbf{Q}_{\text{clk}_{s_n}}\}_{n=1}^N$  have the same form as in (3), except that  $S_{\tilde{w}_{\delta t}}$  and  $S_{\tilde{w}_{\dot{\delta t}}}$  are replaced with the receiver and  $n$ -th base station's clock process noise spectra, respectively. Note that the cross-correlations in  $\bar{\mathbf{Q}}_{\text{clk}}$  come from combining the effect of the receiver and cellular base station clocks in the same state. Since the receiver clock bias is common to all clock states, the cross-correlations in  $\bar{\mathbf{Q}}_{\text{clk}}$  will be the receiver clock's process noise covariance [35].

The measurement vector defined by  $\mathbf{z}(k) \triangleq [z_{\text{alt}}(k), z_1(k), \dots, z_N(k)]^\top$  is used to estimate  $\mathbf{x}$  in the EKF. In vector form, the measurement equation is given by

$$\mathbf{z}(k) = \mathbf{h}[\mathbf{x}(k)] + \mathbf{v}(k), \quad (6)$$

where  $\mathbf{h}[\mathbf{x}(k)]$  is a vector-valued function defined as  $\mathbf{h}[\mathbf{x}(k)] \triangleq [h_{\text{alt}}[\mathbf{x}(k)], h_1[\mathbf{x}(k)], \dots, h_N[\mathbf{x}(k)]]^\top$  with  $h_{\text{alt}}[\mathbf{x}(k)] = z_r(k) + v_{\text{alt}}(k)$ ,  $h_n[\mathbf{x}(k)] \triangleq \|\mathbf{r}_r(k) - \mathbf{r}_{s_n}\|_2 + c\delta t_n(k)$ , and  $\mathbf{v}(k) \triangleq [v_{\text{alt}}(k), v_1(k), \dots, v_N(k)]^\top$  is the measurement noise vector, which is modeled as zero-mean white Gaussian random vector with covariance  $\mathbf{R}(k) \triangleq \text{diag}[\sigma_{\text{alt}}^2(k), \sigma_1^2(k), \dots, \sigma_N^2(k)]$ .

An EKF is implemented given the dynamics and measurement models in (5) and (6) to produce an estimate of  $\mathbf{x}(k)$  using all measurements up to time-step  $k$ , denoted by  $\hat{\mathbf{x}}(k|k)$ , and an associated estimation error covariance denoted by  $\mathbf{P}(k|k)$ . The EKF is initialized from two successive position priors according to the framework discussed in [35]. The EKF process and measurement noise covariances are described in the next subsection.

## B. EKF Settings

The measurement rate was  $T = 0.08/3$  s; the jerk process noise spectra were chosen to be  $\tilde{q}_N = 18 \text{ m}^2/\text{s}^5$ ,  $\tilde{q}_E = 18 \text{ m}^2/\text{s}^5$ , and  $\tilde{q}_D = 0.5 \text{ m}^2/\text{s}^5$ ; and the receiver and base station clock process noise covariance matrices were chosen to be

$$\mathbf{Q}_{\text{clk},r} = \begin{bmatrix} 9.57 \times 10^{-5} & 2.52 \times 10^{-8} \\ 2.52 \times 10^{-8} & 1.89 \times 10^{-6} \end{bmatrix}, \quad (7)$$

$$\mathbf{Q}_{\text{clk},s_n} = \begin{bmatrix} 3.11 \times 10^{-7} & 2.52 \times 10^{-11} \\ 2.52 \times 10^{-11} & 1.89 \times 10^{-9} \end{bmatrix}. \quad (8)$$

The above clock process noise covariance matrices assumed the receiver to be equipped with a typical temperature-compensate crystal oscillator (TCXO), while the cellular base stations are equipped with a typical oven-controlled crystal oscillator (OCXO) [8].

The altimeter measurement error variance  $\sigma_{\text{alt}}^2(k)$  was assumed to be  $5 \text{ m}^2$ . The cellular measurement noise variances were calculated as a function of the CNR and receiver parameters as discussed in [33], [34]. The range of values taken by the measurement noise variances are explicitly stated for each region in Section V.

## IV. EXPERIMENTAL SETUP AND FLIGHT REGIONS

This section overviews the experimental setup used for data collection and processing. It also describes the flight regions.

### A. Hardware and Software Setup

The C-12 aircraft was equipped with a universal software radio peripheral (USRP) with consumer-grade cellular antennas to sample three cellular bands and store the samples on a desktop computer for off-line processing. The stored samples were post-processed with the 3G and 4G cellular modules of MATRIX. The SDR produces navigation observables: Doppler frequency, carrier phase, and pseudorange, along with corresponding CNRs. The hardware setup is shown in Fig. 1.

The aircraft's ground-truth trajectory was taken from the C-12's on-board Honeywell H764-ACE EGI INS/GPS, which provided time-space-position information (TSPI) at a 1 Hz data rate. The accuracy specifications are tabulated in Table I.

TABLE I  
HONEYWELL H764-ACE EGI ACCURACY

Metric	Blended INS/GPS Accuracy
Position	5 m, spherical error probable (SEP)
Velocity	0.01 m/s
Heading	0.015 deg
Pitch/Roll	0.01 deg

### B. Flight Regions

Three flights are reported in this article, each of which took place in one of three regions: (i) Region A: a rural region in Edwards AFB, California, (ii) Region B: a semi-urban region in Palmdale, California, and (iii) Region C: an urban region in Riverside, California. Different maneuvers were planned over the three regions to test several aspects of aircraft navigation with cellular SOPs.

Fig. 2 shows the regions in which the experiments were performed as well as the aircraft trajectory for each flight. The 3G base transceiver stations (BTSs) and 4G eNodeBs were mapped via the method described in [36]. The mapped towers were cross-checked via Google Earth and online databases and are shown in Fig. 2. This article investigates the potential of cellular SOPs for navigation; therefore, mapping the SOPs will not be discussed.

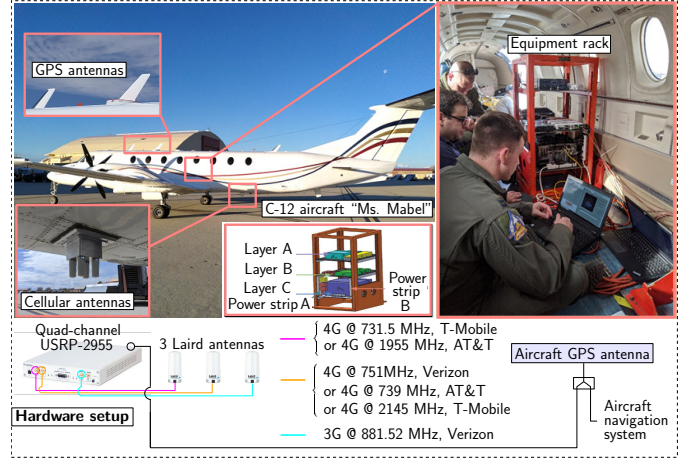


Fig. 1. Hardware setup with which the C-12 aircraft was equipped.

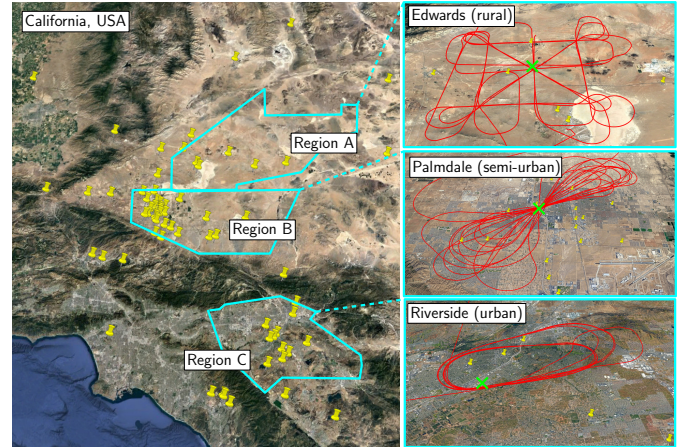


Fig. 2. Regions A, B, and C in which the flight campaigns took place. The yellow pins represent 3G and 4G cellular towers that were mapped and analyzed in this study. The right figures show the aircraft trajectory in all regions (shown in red). Geographic points of interest in each region, shown in green crosses, were chosen according to the designed trajectories.

## V. AERIAL NAVIGATION RESULTS

This section presents experimental results demonstrating high-altitude aircraft navigation using the framework discussed in Section II in the three regions shown in Fig. 2.

### A. Aerial Navigation in Region A

The test trajectory in Region A consisted of (i) a 24-km straight segment, followed by (ii) a  $270^\circ$  banking turn of length 18 km, and (iii) a final 9-km straight segment.

The total distance traveled by the aircraft was over 51 km, completed in 9 minutes. The aircraft maintained an altitude of approximately 5,000 ft AGL throughout the trajectory. During this flight, three radio frequency channels were sampled at: (i) 881.52 MHz, which is a 3G channel allocated for the U.S. cellular provider Verizon Wireless, (ii) 731.5 MHz, a 4G LTE channel allocated for T-Mobile, and (iii) 751 MHz, also a 4G LTE channel allocated for Verizon. A total of 11 cellular SOPs were heard during the experiment: (a) six 3G BTSs and (b) five 4G eNodeBs. The 11 cellular SOPs were acquired at different times and tracked for different durations based on signal quality. Figs. 3(a)–(c) show the time history of (i) measured CNRs, (ii) pseudorange measurements, and (iii) pseudorange error (pseudorange minus the true range), for all 11 cellular SOPs, respectively. One can see from Fig. 3(c) that pseudorange tracking is lost for some of the cellular SOPs at or around 300 s, which is when the aircraft starts banking to perform the 270° turn. In addition to the high dynamics of the banking turn, it is suspected that the aircraft’s wings and body block or severely attenuate some of the signals during banking, causing loss of tracking. Using the expressions of the measurement noise variances as a function of the CNR and receiver parameters in [33], [34],  $\sigma_n(k)$  was found to vary between 1.44 to 9.47 m.

Next, the state vector  $\mathbf{x}$  of the aircraft was estimated using the carrier phase measurements obtained from the cellular SOP receivers via the EKF discussed in Section III-A. The total position RMSE was calculated to be 10.5 m over the 51 km trajectory, traversed in 9 minutes. Fig. 4 shows the aircraft’s true and estimated trajectories. Fig. 5 shows the EKF estimation error plots and corresponding sigma-bounds for the aircraft’s position and velocity states. It is important to note that the position error in the EKF is the largest during the turn. This is due to (i) the measurement errors due to the high dynamics of the banking turn, which severely stressed the tracking loops and (ii) the mismatch in the dynamics model assumed in the EKF, since a 270° banking turn has significantly different dynamics than the assumed continuous Wiener process acceleration model. However, as mentioned earlier, the purpose of this study is to highlight the minimum performance that can be achieved with cellular SOPs. It is important to note that the average distance between the aircraft and the BTSs or eNodeBs was around 30 km over the entire trajectory, with eNodeB 4 being tracked at a 100 km distance in the first part of the trajectory.

### B. Aerial Navigation in Region B

The test trajectory in Region B consisted of (i) an approach to William J Fox Airport, followed by (ii) a touch and go. The total distance traveled by the aircraft was over 57 km completed in 11 minutes. The aircraft descended from an altitude of 7,000 ft AGL. During this flight, three radio frequency channels were sampled at: (i) 881.52 MHz, which is a 3G channel allocated for the U.S. cellular provider Verizon Wireless, (ii) 731.5 MHz, a 4G LTE channel allocated for T-Mobile, and (iii) 739 MHz, also a 4G LTE channel allocated for AT&T. A total of 14 cellular SOPs were heard during the

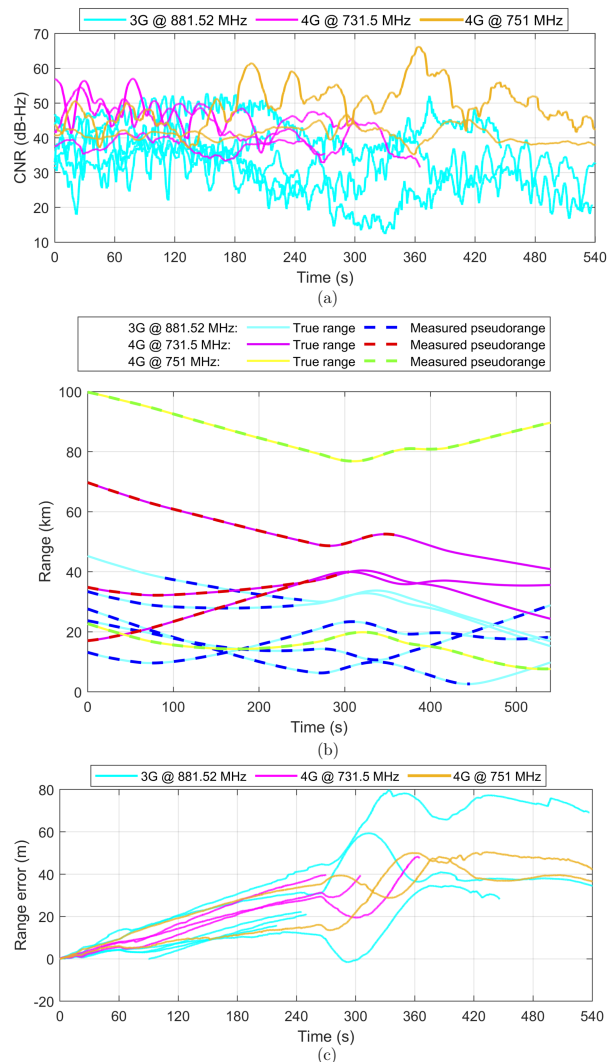


Fig. 3. (a) Time history of the CNRs for all the base stations used to compute the navigation solution in Region A. (b) Time history of the pseudoranges estimated by the cellular SOP receivers and the corresponding true range in Region A. The initial values of the pseudoranges and ranges were subtracted out for ease of comparison. (c) Time history of the pseudorange error (pseudorange minus the true range) for all cellular SOPs in Region A. The error is driven by a common term, which is the receiver’s clock bias. The errors increase significantly at around 300 s, which is when the turn starts. The high dynamics of a banking turn inject stress on the tracking loops. The initial values of the pseudorange errors were subtracted out for ease of comparison.

experiment: (a) nine 3G BTSs and (b) five 4G eNodeBs. The 14 cellular SOPs were acquired at different times and tracked for different durations based on signal quality. Figs. 6(a)–(c) show the time history of (i) measured CNRs, (ii) pseudorange measurements, and (iii) pseudorange error (pseudorange minus the true range), for all 14 cellular SOPs, respectively. Using the expressions of the measurement noise variances as a function of the CNR and receiver parameters in [33], [34],  $\sigma_n(k)$  was found to vary between 1.3 to 4.43 m.

Next, the state vector  $\mathbf{x}$  of the aircraft was estimated using the carrier phase measurements obtained from the cellular SOP receivers via the EKF discussed in Section III-A. The total position RMSE was calculated to be 4.95 m over the 57 km trajectory, traversed in 11 minutes. Fig. 7 shows the

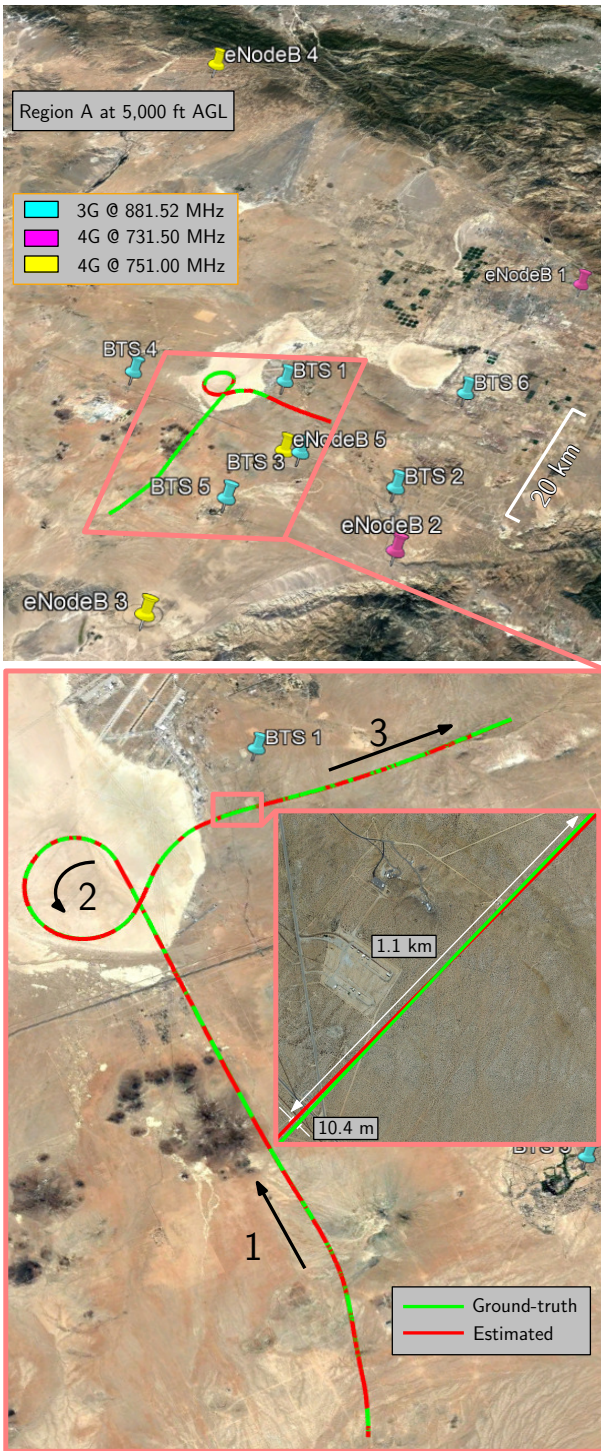


Fig. 4. Experimental layout and results in Region A showing: (i) BTS and eNodeB positions, (ii) true aircraft trajectory, and (iii) aircraft trajectory estimated exclusively using cellular SOPs. The aircraft traversed a total distance of 51 km traversed in 9 minutes during the experiment. The position RMSE over the entire trajectory was found to be 10.5 m.

aircraft’s true and estimated trajectories. Fig. 8 shows the EKF estimation error plots and corresponding sigma-bounds for the aircraft’s position and velocity states. It is important to note that the aircraft’s position estimate on touchdown is less than 3 m away from the true position and is well within the runway. In addition, the geometric diversity becomes poor after the

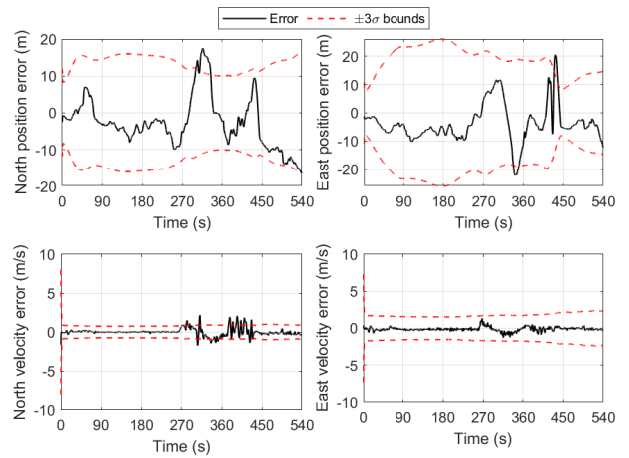


Fig. 5. EKF plots showing the time history of the position and velocity errors in Region A as well as the  $\pm 3\sigma$  bounds. As expected, the EKF performs poorly in the second leg, where the mismatch between the true aircraft dynamics and the assumed EKF model is highest.

sixth minute as the aircraft is flying on one side of the SOPs. This explains the increasing sigma-bounds in Fig. 8.

### C. Aerial Navigation in Region C

The test trajectory in Region C consisted of a holding pattern over Riverside Municipal Airport. The total distance traveled by the aircraft was over 55 km, completed in 8.5 minutes. The aircraft maintained an altitude of approximately 15,000 ft AGL throughout the trajectory. During this flight, two radio frequency channels were sampled at: (i) 881.52 MHz, which is a 3G channel allocated for the U.S. cellular provider Verizon Wireless, (ii) 1955 MHz, a 4G LTE channel allocated for AT&T, and (iii) (ii) 2145 MHz, a 4G LTE channel allocated for T-Mobile. A total of 11 cellular SOPs were heard during the experiment: (a) seven 3G BTSs and (b) four 4G eNodeBs. The 11 cellular SOPs were acquired at different times and tracked for different durations based on signal quality. Figs. 9(a)–(c) show the time history of (i) measured CNRs, (ii) pseudorange measurements, and (iii) pseudorange error (pseudorange minus the true range), for all 9 cellular SOPs, respectively. Similar to the first flight, one can see from Fig. 9(c) that pseudorange tracking is lost for some of the cellular SOPs when the aircraft starts banking to perform the turns in the holding pattern. Using the expressions of the measurement noise variances as a function of the CNR and receiver parameters in [33], [34],  $\sigma_n(k)$  was found to vary between 1.73 to 5.69 m.

Next, the state vector  $\mathbf{x}$  of the aircraft was estimated using the carrier phase measurements obtained from the cellular SOP receivers via the EKF discussed in Section III-A. The total position RMSE was calculated to be 15.44 m over the 55 km trajectory, traversed in 8.5 minutes. Fig. 10 shows the aircraft’s true and estimated trajectories. Fig. 11 shows the EKF estimation error plots and corresponding sigma-bounds for the aircraft’s position and velocity states. As expected, the measurement errors and the mismatch in the dynamics model assumed in the EKF are more severe during the turns.

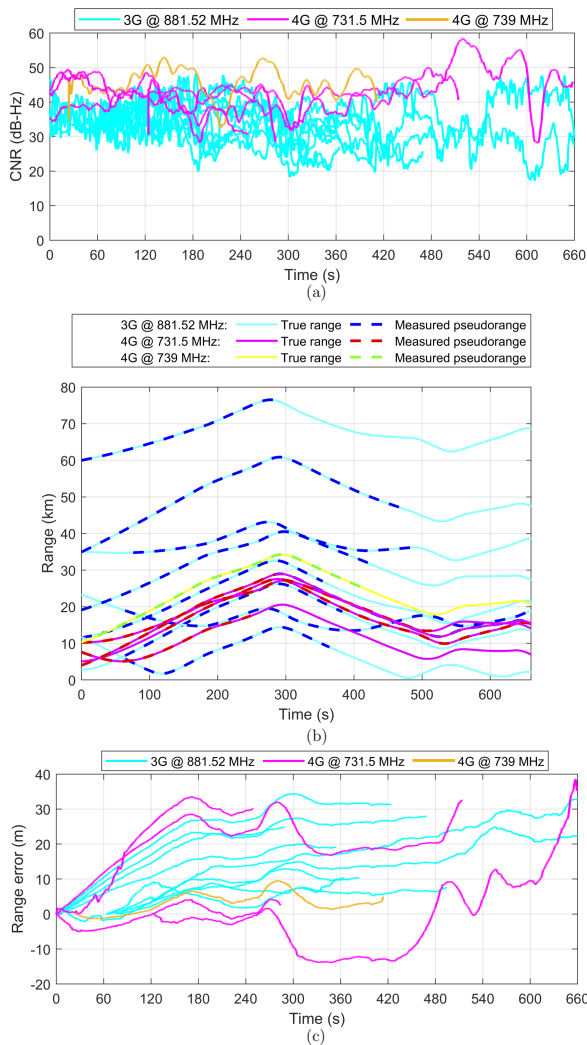


Fig. 6. (a) Time history of the CNRs for all the base stations used to compute the navigation solution in Region B. (b) Time history of the pseudoranges estimated by the cellular SOP receivers and the corresponding true range in Region B. The initial values of the pseudoranges and ranges were subtracted out for ease of comparison. (c) Time history of the pseudorange error (pseudorange minus the true range) for all cellular SOPs in Region B.

D. Discussion

The navigation performance in all three Regions is summarized in Table II.

TABLE II  
NAVIGATION PERFORMANCE WITH CELLULAR SIGNALS

Metric	Region A	Region B	Region C
Cellular towers {3G, 4G}	{6, 5}	{9, 5}	{7, 4}
Cellular frequencies (MHz)	881.52	881.52	881.52
	731.5	731.5	1955
	751	739	2145
Flight duration (mins)	9	11	8.5
Flight length (km)	51	57	55
Altitude AGL (ft)	5,000	0 – 7,000	15,000
Position RMSE (m)	10.53	4.96	11.67
Velocity RMSE (m/s)	0.58	0.50	0.71
Maximum position error (m)	22.67	15.04	25.89
Maximum velocity error (m/s)	2.29	3.19	3.94

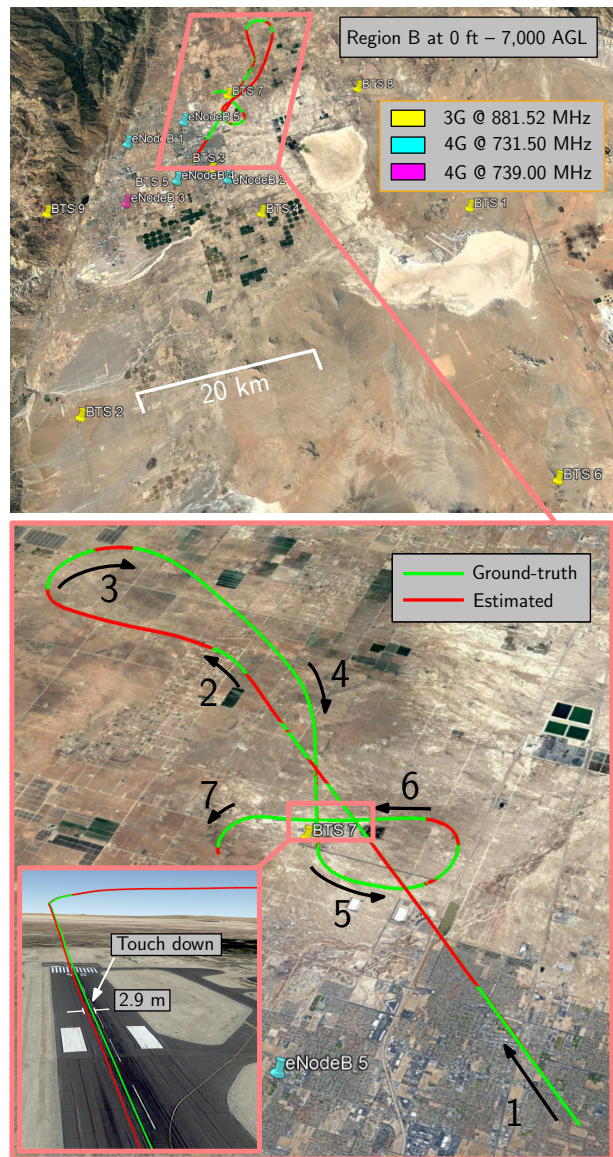


Fig. 7. Experimental layout and results in Region B showing: (i) BTS and eNodeB positions, (ii) true aircraft trajectory, and (iii) aircraft trajectory estimated exclusively using cellular SOPs. The aircraft traversed a total distance of 57 km traversed in 11 minutes during the experiment. The position RMSE over the entire trajectory was found to be 4.96 m. Note that the position estimate on touchdown is less than 3 m away from the true aircraft position and is well within the runway.

The achieved results unveiled the remarkable potential of utilizing cellular SOPs for sustained accurate high altitude aircraft navigation. The results presented herein, although promising, can be further improved upon in several ways. The following are key takeaways and design consideration for reliable aircraft navigation with cellular SOPs.

- Accounting for the aircraft dynamical model mismatch: Aircraft, such as the C-12, can perform a variety of highly dynamic maneuvers. The dynamics model employed in the EKF in this study did not perfectly capture the aircraft dynamics throughout its trajectory, leading to increased estimation error due to the mismatch between the actual aircraft’s dynamics and the dynamical model assumed by the EKF. This mismatch can be mitigated

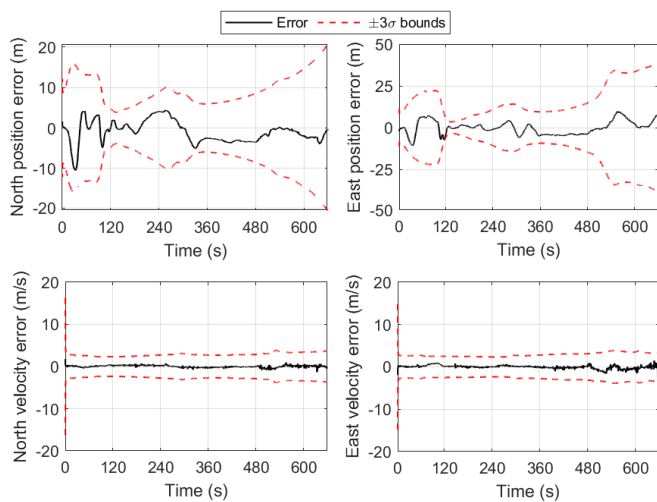


Fig. 8. EKF plots showing the time history of the position and velocity errors in Region B as well as the  $\pm 3\sigma$  bounds.

by using appropriate dynamical models for fixed-wing aircraft or more elaborate dynamical models (e.g., Wiener process acceleration, Singer acceleration, mean-adaptive acceleration, semi-Markov jump process, circular motion, curvilinear motion, coordinated turn, among others [30]) coupled with adaptive estimation techniques [37]–[42]. Alternatively, if access to raw IMU data is available, a kinematic model with IMU measurements can be used, as is the case with most INS aiding techniques [10], [31].

- Accounting for statistical model mismatch: The aircraft’s process noise covariance assumed by the EKF’s dynamical model was found via off-line tuning and by analyzing the aircraft’s maneuvers from ground truth data. In addition, the process noise covariances of the aircraft’s receiver clock was set at typical TCXO values and the cellular SOP transmitter clocks were set at typical OCXO values. While these values represent good approximations for the aircraft’s receiver clock quality as well as the quality of typical cellular SOP transmitters, mismatches between the assumed values and the actual values can be mitigated via adaptive estimation techniques [43]–[45], which would improve the estimation performance. Adaptive estimation techniques would also mitigate the errors arising from mismatches between the actual measurement noise variances and calculated measurement noise variances.
- Vertical dilution of precision: At high altitudes, there is very little vertical diversity with respect to terrestrial cellular towers. As such, the aircraft’s cellular-based navigation solution VDOP will be large. Nevertheless, the aircraft’s vertical position can still be estimated from the pseudoranges extracted from cellular towers, albeit with less accuracy compared to the results presented in this paper, which fused altimeter-based measurements.
- Mapping cellular SOPs: This article assumed cellular SOPs to be mapped *a priori*. This was achieved via a mapping campaign according to the method described in [36]. Nevertheless, such assumption can be relaxed via

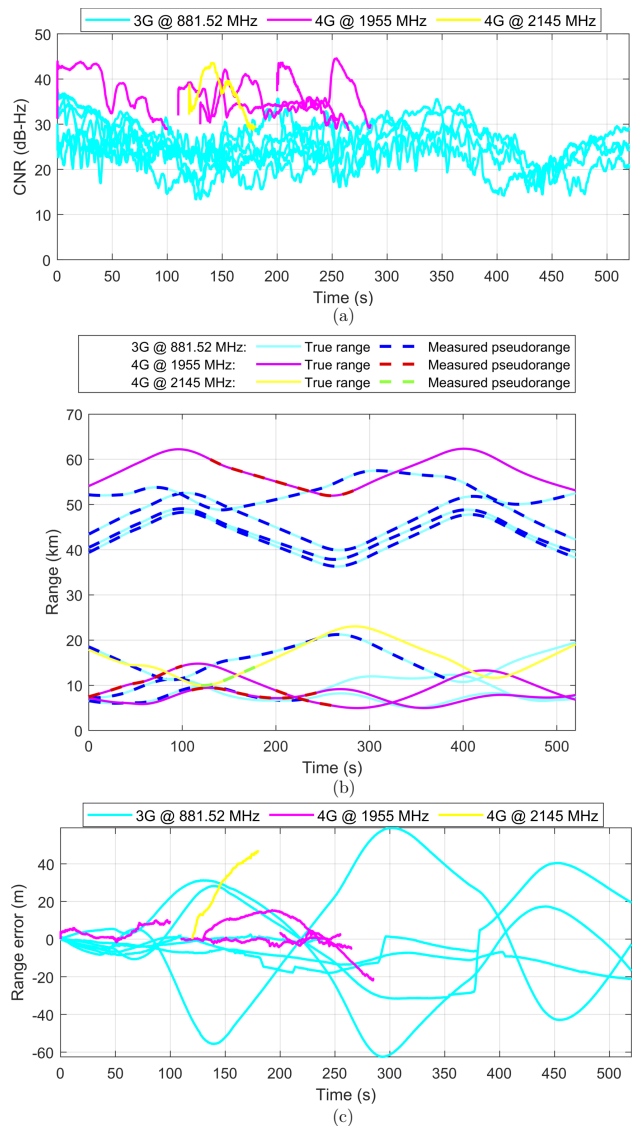


Fig. 9. (a) Time history of the CNRs for all the base stations used to compute the navigation solution in Region C. (b) Time history of the pseudoranges estimated by the cellular SOP receivers and the corresponding true range in Region C. The initial values of the pseudoranges and ranges were subtracted out for ease of comparison. (c) Time history of the pseudorange error (pseudorange minus the true range) for all cellular SOPs in Region C. The error is driven by a common term, which is the receiver’s clock bias.

the radio simultaneous localization and mapping (radio SLAM) framework, which maps the unknown SOPs simultaneously with localizing the aircraft [14], [31].

## VI. CONCLUSION

This article demonstrated robust high altitude aircraft navigation with 3G CDMA and 4G LTE cellular SOPs. An EKF was used to fuse cellular carrier phase measurements to estimate the aircraft’s position, velocity, and time. The EKF utilized a simple, yet effective continuous Wiener process acceleration model to describe the aircraft dynamics. A multitude of flight trajectories and altitudes above ground level (AGL) were exercised in the three flights: (i) a 51 km trajectory of grid maneuvers with banking and straight segments at about 5,000 ft AGL, (ii) a 57 km trajectory of a teardrop descent

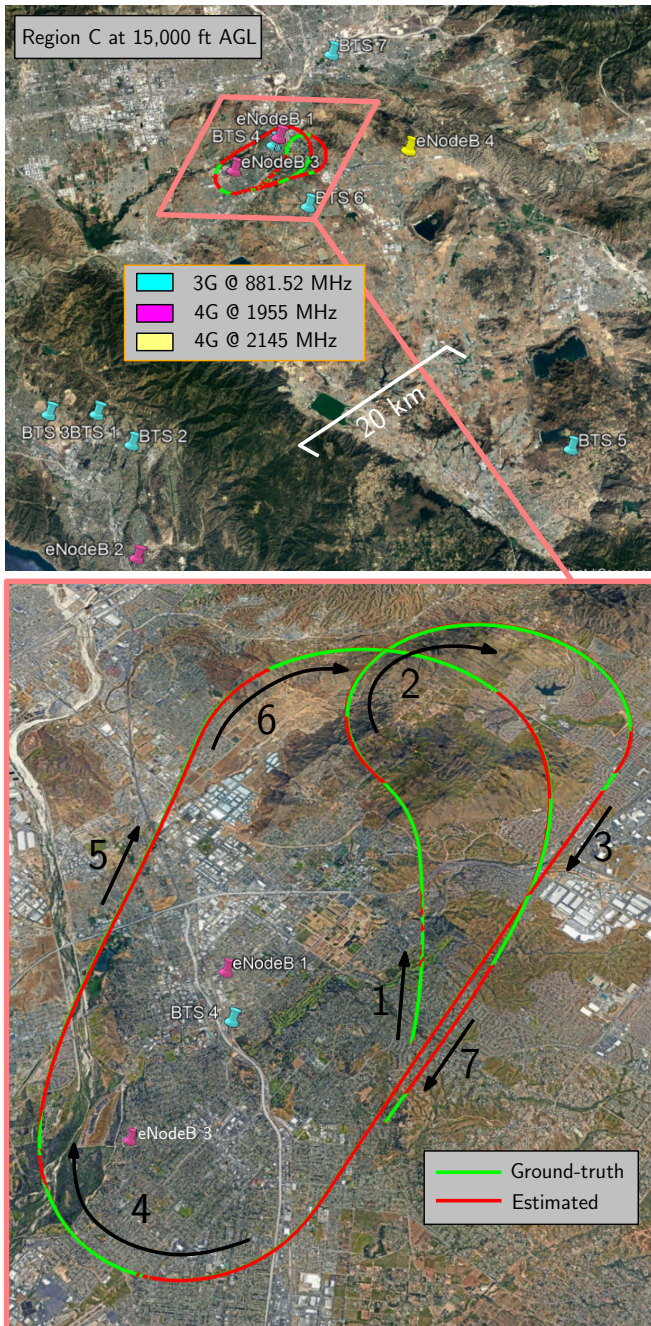


Fig. 10. Experimental layout and results in Region C showing: (i) BTS and eNodeB positions, (ii) true aircraft trajectory, and (iii) aircraft trajectory estimated exclusively using cellular SOPs. The aircraft traversed a total distance of 55 km traversed in 8.5 minutes during the experiment. The position RMSE over the entire trajectory was found to be 15.44 m.

from 7,000 ft AGL down to touchdown at the runway, and (iii) a 55 km trajectory of a holding pattern at about 15,000 ft AGL. Cellular SOPs produced remarkable navigation accuracy in all three flights, achieving a 3-D position RMSE of 10.53 m, 4.96 m, and 15.44 m, respectively. These unprecedented results demonstrate the potential of cellular signals as a viable alternative to GNSS for high altitude aircraft navigation. While the presented are encouraging, more accurate navigation results can be achieved by fusing cellular SOP observables with an INS.

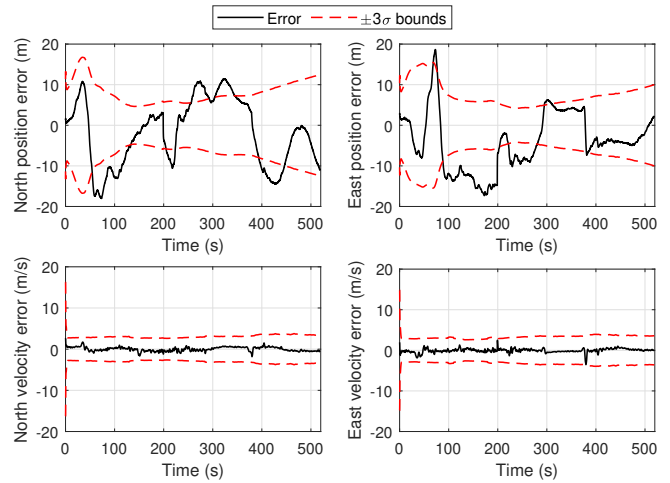


Fig. 11. EKF plots showing the time history of the position and velocity errors in Region C as well as the  $\pm 3\sigma$  bounds. As expected, the EKF performs poorly in the second leg, where the mismatch between the true aircraft dynamics and the assumed EKF model is highest.

#### ACKNOWLEDGMENTS

The authors would like to thank Edwards AFB and Holloman AFB for inviting the ASPIN Laboratory to conduct experiments on Air Force aircraft in the “SNIFFER: Signals of opportunity for Navigation In Frequency-Forbidden EnviRonments” flight campaign. The authors would like to thank Joshua Morales, Kimia Shamaei, Mahdi Maaref, Kyle Semelka, MyLinh Nguyen, and Trier Mortlock for their help with preparing for data collection. DISTRIBUTION STATEMENT A. Approved for public release; Distribution is unlimited. 412TW-PA-20146.

#### REFERENCES

- [1] ASRS/NASA, “ASRS Database Online,” <https://asrs.arc.nasa.gov/search/database.html>.
- [2] M. Harris, “FAA files reveal a surprising threat to airline safety,” *IEEE Spectrum Online*. <https://spectrum.ieee.org/faa-files-reveal-a-surprising-threat-to-airline-safety-the-us-militarys-gps-tests>, January 2021.
- [3] D. Miralles, A. Bornot, P. Rouquette, N. Levisne, D. Akos, Y.-H.Chen, S. Lo, and T. Walter, “An assessment of GPS spoofing detection via radio power and signal quality monitoring for aviation safety operations,” *IEEE Intelligent Transportation Systems Magazine*, vol. 12, no. 3, pp. 136–146, June 2020.
- [4] F. Doyis, L. Ruotsalainen, R. Toledo-Moreo, Z. Kassas, and V. Gikas, “Recent advancement on the use of global navigation satellite system-based positioning for intelligent transport systems,” *IEEE Intelligent Transportation Systems Magazine*, vol. 12, no. 3, pp. 6–9, June 2020.
- [5] International Civil Aviation Organization (ICAO), “An urgent need to address harmful interferences to GNSS,” <https://www.iata.org/contentassets/e45e5219cc8c4277a0e80562590793da/address-harmful-interferences-gnss.pdf>, Tech. Rep., May 2019.
- [6] A. Hansen, S. Mackey, H. Wassaf, E. Wallischek, C. Scarpone, M. Barzach, and E. Baskerville, “Complementary PNT and GPS backup technologies demonstration report: Sections 1 through 10,” *John A. Volpe National Transportation Systems Center (US)*, no. DOT-VNTSC-20-07, 2021.
- [7] M. Bartock, J. Brule, Y. Li-Baboud, S. Lightman, J. McCarthy, K. Reczek, D. Northrip, A. Scholz, and T. Suloway, “Foundational PNT profile: Applying the cybersecurity framework for the responsible use of positioning, navigation, and timing (PNT) services,” *National Institute of Standards and Technology (NIST)*, no. NISTIR 8323, February 2021.
- [8] Z. Kassas, “Position, navigation, and timing technologies in the 21st century,” J. Morton, F. van Diggelen, J. Spilker, Jr., and B. Parkinson, Eds. Wiley-IEEE, 2021, vol. 2, ch. 38: Navigation with Cellular Signals of Opportunity, pp. 1171–1223.

- [9] A. Abdallah, J. Khalife, and Z. Kassas, "Experimental characterization of received 5G signals carrier-to-noise ratio in indoor and urban environments," in *Proceedings of IEEE Vehicular Technology Conference*, April 2021, pp. 1–5.
- [10] Z. Kassas, M. Maaref, J. Morales, J. Khalife, and K. Shamaei, "Robust vehicular localization and map matching in urban environments through IMU, GNSS, and cellular signals," *IEEE Intelligent Transportation Systems Magazine*, vol. 12, no. 3, pp. 36–52, June 2020.
- [11] M. Maaref and Z. Kassas, "Autonomous integrity monitoring for vehicular navigation with cellular signals of opportunity and an IMU," *IEEE Transactions on Intelligent Transportation Systems*, vol. 23, no. 6, pp. 5586–5601, June 2022.
- [12] J. Khalife and Z. Kassas, "On the achievability of submeter-accurate UAV navigation with cellular signals exploiting loose network synchronization," *IEEE Transactions on Aerospace and Electronic Systems*, vol. 58, no. 5, pp. 4261–4278, October 2022, doi: 10.1109/TAES.2022.3162770.
- [13] J. Khalife and Z. Kassas, "Differential framework for submeter-accurate vehicular navigation with cellular signals," *IEEE Transactions on Intelligent Vehicles*, 2022, accepted, doi: 10.1109/TIV.2022.3187957.
- [14] Z. Kassas, J. Khalife, A. Abdallah, and C. Lee, "I am not afraid of the GPS jammer: resilient navigation via signals of opportunity in GPS-denied environments," *IEEE Aerospace and Electronic Systems Magazine*, vol. 37, no. 7, pp. 4–19, July 2022, doi: 10.1109/MAES.2022.3154110.
- [15] Y. Zeng, Q. Wu, and R. Zhang, "Accessing from the sky: A tutorial on UAV communications for 5G and beyond," *Proceedings of the IEEE*, vol. 107, no. 12, pp. 2327–2375, December 2019.
- [16] X. Cai, J. Rodriguez-Pineiro, X. Yin, N. Wang, B. Ai, G. Pedersen, and A. Yuste, "An empirical air-to-ground channel model based on passive measurements in LTE," *IEEE Transactions on Vehicular Technology*, vol. 68, no. 2, pp. 1140–1154, February 2019.
- [17] W. Khawaja, I. Guvenc, D. Matolak, U. Fiebig, and N. Schneckenburger, "A survey of air-to-ground propagation channel modeling for unmanned aerial vehicles," *IEEE Communications Surveys & Tutorials*, vol. 21, no. 3, pp. 2361–2391, 2019, doi: 10.1109/COMST.2019.2915069.
- [18] K. Matheou, R. Apaza, A. Downey, R. Kerczewski, J. Jung, C. Ippolito, and H. Modi, "Analysis of at-altitude LTE power spectra for small unmanned aircraft system C2 communications," in *Proceedings of Integrated Communications, Navigation and Surveillance Conference*, April 2019, pp. 1–12.
- [19] X. Cai, N. Wang, J. Rodriguez-Pineiro, X. Yin, A. Yuste, W. Fan, G. Zhang, G. Pedersen, and L. Tian, "Low altitude air-to-ground channel characterization in LTE network," in *Proceedings of European Conference on Antennas and Propagation*, April 2019, pp. 1–5.
- [20] B. Van Der Bergh, A. Chiumento, and S. Pollin, "LTE in the sky: trading off propagation benefits with interference costs for aerial nodes," *IEEE Communications Magazine*, vol. 54, no. 5, pp. 44–50, May 2016.
- [21] I. Kovacs, R. Amorim, H. Nguyen, J. Wigard, and P. Mogensen, "Interference analysis for UAV connectivity over LTE using aerial radio measurements," in *Proceedings of IEEE Vehicular Technology Conference*, September 2017, pp. 1–6.
- [22] R. Amorim, J. Wigard, I. Kovacs, and T. Sorensen, "UAV communications for 5G and beyond," Y. Zeng, I. Guvenc, R. Zhang, G. Geraci, and D. Matolak, Eds. Wiley-IEEE, 2021, ch. 5: Performance Enhancements for LTE-Connected UAVs: Experiments and Simulations, pp. 139–161.
- [23] E. Teng, J. Diogo Falcao, and B. Iannucci, "Holes-in-the-sky: A field study on cellular-connected UAS," in *Proceedings of International Conference on Unmanned Aircraft Systems*, June 2017, pp. 1165–1174.
- [24] X. Lin, V. Yajnanarayana, S. Muruganathan, S. Gao, H. Asplund, H. Maattanen, M. Bergstrom, S. Euler, and Y. Wang, "The sky is not the limit: LTE for unmanned aerial vehicles," *IEEE Communications Magazine*, vol. 56, no. 4, pp. 204–210, April 2018.
- [25] G. Athanasiadou, M. Batistatos, D. Zarbouti, and G. Tsoulos, "LTE ground-to-air field measurements in the context of flying relays," *IEEE Wireless Communications*, vol. 26, no. 1, pp. 12–17, February 2019.
- [26] A. Abdalla and V. Marojevic, "Communications standards for unmanned aircraft systems: The 3GPP perspective and research drivers," *IEEE Communications Standards Magazine*, vol. 5, no. 1, pp. 70–77, March 2021.
- [27] H. Maattanen, "UAV communications for 5G and beyond," Y. Zeng, I. Guvenc, R. Zhang, G. Geraci, and D. Matolak, Eds. Wiley-IEEE, 2021, ch. 6: 3GPP Standardization for Cellular-Supported UAVs, pp. 163–180.
- [28] E. Kim and Y. Shin, "Feasibility analysis of LTE-based UAS navigation in deep urban areas and DSRC augmentation," *Sensors*, vol. 19, no. 9, pp. 4192–4207, April 2019, doi: 10.3390/s19194192.
- [29] Z. Kassas, J. Khalife, A. Abdallah, C. Lee, J. Jurado, S. Wachtel, J. Duede, Z. Hoeffner, T. Hulsey, R. Quirarte, and R. Tay, "Assessment of cellular signals of opportunity for high altitude aircraft navigation," *IEEE Aerospace and Electronic Systems Magazine*, vol. 37, no. 10, pp. 4–19, October 2022, doi: 10.1109/MAES.2022.3187142.
- [30] X. Li and V. Jilkov, "Survey of maneuvering target tracking. Part I: Dynamic models," *IEEE Transactions on Aerospace and Electronic Systems*, vol. 39, no. 4, pp. 1333–1364, 2003, doi: 10.1109/TAES.2003.1261132.
- [31] J. Morales and Z. Kassas, "Tightly-coupled inertial navigation system with signals of opportunity aiding," *IEEE Transactions on Aerospace and Electronic Systems*, vol. 57, no. 3, pp. 1930–1948, 2021.
- [32] J. Barnes, A. Chi, R. Andrew, L. Cutler, D. Healey, D. Leeson, T. McGunigal, J. Mullen, W. Smith, R. Sydnor, R. Vessot, and G. Winkler, "Characterization of frequency stability," *IEEE Transactions on Instrumentation and Measurement*, vol. 20, no. 2, pp. 105–120, May 1971.
- [33] J. Khalife, K. Shamaei, and Z. Kassas, "Navigation with cellular CDMA signals – part I: Signal modeling and software-defined receiver design," *IEEE Transactions on Signal Processing*, vol. 66, no. 8, pp. 2191–2203, April 2018.
- [34] K. Shamaei and Z. Kassas, "LTE receiver design and multipath analysis for navigation in urban environments," *NAVIGATION, Journal of the Institute of Navigation*, vol. 65, no. 4, pp. 655–675, December 2018.
- [35] J. Khalife and Z. Kassas, "Opportunistic UAV navigation with carrier phase measurements from asynchronous cellular signals," *IEEE Transactions on Aerospace and Electronic Systems*, vol. 56, no. 4, pp. 3285–3301, August 2020, doi: 10.1109/TAES.2019.2948452.
- [36] J. Morales and Z. Kassas, "Optimal collaborative mapping of terrestrial transmitters: receiver placement and performance characterization," *IEEE Transactions on Aerospace and Electronic Systems*, vol. 54, no. 2, pp. 992–1007, April 2018.
- [37] M. Yeddanapudi, Y. Bar-Shalom, and K. Pattipati, "IMM estimation for multitarget-multisensor air traffic surveillance," *Proceedings of the IEEE*, vol. 85, no. 1, pp. 80–96, January 1997.
- [38] A. Mohamed and K. Schwarz, "Adaptive Kalman filtering for INS/GPS," *Journal of Geodesy*, vol. 73, no. 4, pp. 193–203, 1999.
- [39] P. Hanlon and P. Maybeck, "Multiple-model adaptive estimation using a residual correlation Kalman filter bank," *IEEE Transactions on Aerospace and Electronic Systems*, vol. 36, no. 2, pp. 393–406, April 2000.
- [40] C. Hide, T. Moore, and M. Smith, "Adaptive Kalman filtering for low-cost INS/GPS," *The Journal of Navigation*, vol. 56, no. 1, pp. 143–152, January 2003.
- [41] W. Ding, J. Wang, C. Rizos, and D. Kinlyside, "Improving adaptive Kalman estimation in GPS/INS integration," *The Journal of Navigation*, vol. 60, no. 3, pp. 517–529, September 2007.
- [42] M. Yu, "INS/GPS integration system using adaptive filter for estimating measurement noise variance," *IEEE Transactions on Aerospace and Electronic Systems*, vol. 48, no. 2, pp. 1786–1792, April 2012.
- [43] Z. Kassas, V. Ghadiok, and T. Humphreys, "Adaptive estimation of signals of opportunity," in *Proceedings of ION GNSS Conference*, September 2014, pp. 1679–1689.
- [44] J. Dunik, O. Straka, O. Kost, and J. Havlik, "Noise covariance matrices in state-space models: A survey and comparison of estimation methods—part i," *International Journal of Adaptive Control and Signal Processing*, vol. 31, no. 11, pp. 1505–1543, May 2017.
- [45] J. Dunik, O. Kost, O. Straka, and E. Blasch, "Navigation and estimation improvement by environmental-driven noise mode detection," in *Proceedings of IEEE/ION Position, Location, and Navigation Symposium*, 2020, pp. 925–932.



**Zaher (Zak) M. Kassas** (zkassas@ieee.org) is a professor at The Ohio State University and director of the Autonomous Systems Perception, Intelligence, and Navigation (ASPIN) Laboratory. He is also director of the U.S. Department of Transportation Center: CARMEN (Center for Automated Vehicle Research with Multimodal Assured Navigation), focusing on navigation resiliency and security of highly automated transportation systems. He received a B.E. in Electrical Engineering from the Lebanese American University, an M.S. in Electrical

and Computer Engineering from The Ohio State University, and an M.S.E. in Aerospace Engineering and a Ph.D. in Electrical and Computer Engineering from The University of Texas at Austin. He is a recipient of the 2018 National Science Foundation (NSF) Faculty Early Career Development Program (CAREER) award, 2019 Office of Naval Research (ONR) Young Investigator Program (YIP) award, 2022 Air Force Office of Scientific Research (AFOSR) YIP award, 2018 IEEE Walter Fried Award, 2018 Institute of Navigation (ION) Samuel Burka Award, and 2019 ION Col. Thomas Thurlow Award. He is a Senior Editor of the IEEE Transactions on Intelligent Vehicles and an Associate Editor of the IEEE Transactions on Aerospace and Electronic Systems and the IEEE Transactions on Intelligent Transportation Systems. His research interests include cyber-physical systems, estimation theory, navigation systems, autonomous vehicles, and intelligent transportation systems.



**Joe Khalife** (S'15-M'20) is a postdoctoral fellow at the University of California, Irvine and member of the Autonomous Systems Perception, Intelligence, and Navigation (ASPIN) Laboratory. He received a B.E. in Electrical Engineering, an M.S. in Computer Engineering from the Lebanese American University and a Ph.D. in Electrical Engineering and Computer Science from the University of California, Irvine. From 2012 to 2015, he was a research assistant at LAU, and has been a member of the ASPIN Laboratory since 2015. He is a recipient of the 2016

IEEE/ION Position, Location, and Navigation Symposium (PLANS) Best Student Paper Award and the 2018 IEEE Walter Fried Award. His research interests include opportunistic navigation, autonomous vehicles, and software-defined radio.



**Ali A. Abdallah** (S'13) is a Ph.D. student in the Department of Electrical Engineering and Computer Science at the University of California, Irvine and a member of the Autonomous Systems Perception, Intelligence, and Navigation (ASPIN) Laboratory. He received a B.E. in Electrical Engineering from the Lebanese American University. He is a recipient of the Best Student Paper Award at the 2020 IEEE/ION Position, Location, and Navigation Symposium (PLANS).



**Chiawei Lee** is an Assistant Professor and Instructor Flight Test Engineer at the U.S. Air Force Test Pilot School. He serves as the Test Management Program Director where he oversees about a dozen student and staff led flight test projects each year. In addition, he is the Chief Test Safety Officer responsible for the safe execution of curriculum and flight test project safety packages. He received a B.S. in Aerospace Engineering from University of California, Los Angeles and a M.S. in Aero/Astro Engineering from Stanford University.



and statistical sensor management for multi-sensor navigation problems.

**Juan Jurado** is a U.S. Air Force Lieutenant Colonel and the Director of Education at the U.S. Air Force Test Pilot School. He holds a B.S. from Texas A&M University, a M.S. from the Air Force Test Pilot School, and M.S. and Ph.D. from the Air Force Institute of Technology. Previously, he served as Director of Engineering for the 413th Flight Test Squadron and oversaw various C-130, V-22, and H-1 flight test programs. His research interests include aircraft performance modeling, online sensor calibration, image processing, visual-inertial navigation,



**Steven Wachtel** is a U.S. Air Force Captain and a Flight Test Engineer, assigned to the 780th Test Squadron, Eglin AFB, FL. He received a B.S. in Mechanical Engineering from The Ohio State University, an M.S. in Flight Test Engineering from the U.S. Air Force Test Pilot School, and an M.S. in Systems Engineering from the Air Force Institute of Technology.



in Engineering from the University of Arkansas and an M.S. in Flight Test Engineering from Air University.

**Jacob Duede** is a Major in the U.S. Air Force. He was trained as a Communication/Navigation/Mission Systems apprentice on C-17 Globemaster II aircraft and stationed at McChord Air Force Base, WA. He graduated from the U.S. Air Force Academy as a commissioned officer with a B.S. in Mechanical Engineering. He attended the Undergraduate Pilot Training at Columbus Air Force Base, MS. In 2020, he graduated from the U.S. Air Force Test Pilot School at Edwards Air Force Base, CA. He is a Senior Pilot with over 2,000 hours and holds an M.S.



**Zachary Hoeffner** is a flight test engineer at the U.S. Air Force. He received a B.S. in Nuclear Engineering from the U.S. Air Force Academy, an M.S. in Flight Test Engineering from the U.S. Air Force Test Pilot School, an M.S. in Engineering Physics and Applied Physics from the Air Force Institute of Technology, and an M.S. in Nuclear Engineering from the Air Force Institute of Technology.



**Thomas Hulsey** is a U.S. Air Force Flight Commander of Operations Engineering. He received a B.S. in Aerospace Engineering from Missouri University of Science and Technology, an M.S. in Aeronautical Engineering from the Air Force Institute of Technology, and an M.S. in Experimental Flight Test Engineering from the United States Air Force Test Pilot School.



**Rachel Quirarte** is a KC-46 and KC-135 programmatic flight commander and test pilot in the 418th Flight Test Squadron in the U.S. Air Force. She received a B.S. in Aeronautical Engineering from the U.S. Air Force Academy, an M.S. in Flight Test Engineering from the U.S. Air Force Test Pilot School, and an M.S. in Mechanical Engineering from Rice University.



**RunXuan Tay** received a B.S. degree in Electrical Engineering from the University California, San Diego and M.S. degree in Flight Test Engineering from the U.S. Air Force Test Pilot School. He is currently a test pilot at Air Warfare Center, Republic of Singapore Air Force, where he works on fixed wing test programs.